Materials Chemistry and Physics 328 (2024) 129964

Contents lists available at ScienceDirect

Materials Chemistry and Physics

journal homepage: www.elsevier.com/locate/matchemphys

The inverse opals of composite ZnO/TiO_2 and TiO_2/ZnO bilayers

Dániel Attila Karajz [a,*], Csenge Anna Fónay [a], Bence Parditka [b], Zoltán Erdélyi [b], Péter Márton [c], Zoltán Hórvölgyi [c], Imre Miklós Szilágyi [a,**]

[a] Department of Inorganic and Analytical Chemistry, Faculty of Chemical Technology and Biotechnology, Budapest University of Technology and Economics, 1111, Müegyetem rkp. 3., Budapest, Hungary
[b] Department of Solid State Physics, Faculty of Sciences and Technology, University of Debrecen, P.O. Box 400, H-4002, Debrecen, Hungary
[c] Department of Physical Chemistry and Materials Science, Centre for Colloid Chemistry, Faculty of Chemical Technology and Biotechnology, Budapest University of Technology and Economics, Budafoki út 6-8, H-1521, Budapest, Hungary

HIGHLIGHTS

- Synthesis of ZnO, TiO_2 and composite layers and inverse opals.
- Investigation of the heat treatments effect on the mono- and bilayers.
- Study of the inverse opals with the insight gained from the reference layers.
- Evaluation of the inverse opals photocatalytic capabilities under UV and visible light irradiation.

ARTICLE INFO

Keywords:
Inverse opal
Atomic layer deposition
Photocatalysis
Composite

ABSTRACT

The inverse opal structure holds a lot of interesting properties that can be exploited for the use of photocatalysis. TiO_2, ZnO, and composite inverse opals were synthesised with the aim of producing a photocatalytic layer and investigating the changes during the preparation of the structure, focusing the annealing of the material during the removal of the sacrificial polystyrene opal template. First, monolayers and bilayers were synthesised using atomic layer deposition on Si substrates, and their structures were explored before and after heat treatment. The composite bilayers showed deformations on the surface under electron microscopy, namely humps and holes. Second, inverse opals were prepared using vertical deposition of polystyrene nanospheres, atomic layer deposition of TiO_2 and ZnO, and heat treatment. The surface and bulk (structural) properties were analysed using water wettability tests, SEM-EDX, XRD, and UV–Vis spectroscopy methods. Photocatalysis experiments were carried out using UV and visible irradiation of rhodamine 6G solution; interestingly, the performance of the ZnO, TiO_2 and composite inverse opals depends on the type of irradiation.

1. Introduction

Inverse opals are widely researched materials in the fields of photonics [1], sensors [2], batteries [3] and catalysis [4–6]. Materials utilising this structure usually have a large specific surface area [7,8] and photonic properties, such as the photonic band gap [9] and the "slow" photon effect [10]. The advantages of inverse opal photocatalysis are derived from two effects of the structure; high surface area and the 'slow' photon effect, which arises from the photonic band gap [11]. The hollow inverse opal structures with repeating pattern of holes provide a large surface area for enhanced catalytic efficiency [12]. The photonic band gap is caused by the structure of the crystal, and the repeating pattern makes an interference effect to the light of a specific wavelength range, which in turn will be fully refracted [13]. On the two edges of the photonic band gap (blue edge and red edge), light travels with lower group velocity; hence the name 'slow' photon effect. This effect increases the light absorptivity and the optical path length [14]. In the literature, the best strategy to utilize the 'slow' photon effect is to coincide the red edge ("slow" photons propagating in the high dielectric phase, semiconductor) with the band gap of the semiconductor. The

* Corresponding author.
** Corresponding author.
E-mail addresses: karajz412@edu.bme.hu (D.A. Karajz), szilagyi.imre.miklos@vbk.bme.hu (I.M. Szilágyi).

https://doi.org/10.1016/j.matchemphys.2024.129964
Received 18 March 2024; Received in revised form 5 September 2024; Accepted 17 September 2024
Available online 30 September 2024

logic is that increasing the optical path of light in the semiconductor will increase the light harvesting, thus making more electron-hole pairs. The fabrication of this coincidence is not easy, since the position of the slow photon effect is dependent on structure and the angle of irradiation, but this was demonstrated in several articles [11,14,15]. However, there is conjecture in the literature about the nature of the 'slow' photon effect, because experiments showed, that coinciding the blue edges ('slow' photons propagating in the low dielectric phase, air/water) with the band gap of the semiconductor can also increase light harvesting to a similar amount [16,17]. To make things more complicated, S. John and coworkers suggest that the optimal structure of inverse opals is to utilize higher order 'slow' light modes [4]. Photocatalytically active materials, such as TiO_2 [18], ZnO [19], SnO_2 [20], WO_3 [21] and Bi_2WO_6 [22] were used to build photonic inverse opals.

In pursuit of increasing the photocatalytic capabilities, producing composites offers a solution to more than one problem. Usually, semiconductor photocatalysis utilizes the electronic band gap to create electron-hole pairs, which can catalyse chemical reactions. Many phenomena can hinder this process, such as recombination and photodegradation [23]. Recombination of the electron and hole is a well-known bottleneck of photocatalysis and one of the best approaches to get around it is heterojunctions [24]. Heterojunctions help to lower the rate of recombination due to the separation of charges between the two semiconductor band gap systems [25]. This is also true for ZnO and TiO_2 formed heterojunctions because their band gaps are close to each other energy wise, which makes the electron and hole easily transferable between the two semiconductors [26,27]. Furthermore, charge transfer between the two semiconductors works if ZnO [28] or TiO_2 [29] is excited by irradiation. Another problem with several non-Vis absorbing semiconductors, such as anatase TiO_2 with band gap of 3.2 eV [30] or ZnO with a similar 3.37 eV band gap [31], is that their band gap is in the UV region, hence it cannot use the full potential of natural sunlight [32]. In this case, composite materials can increase the visible light absorbance of the material taking advantage of heterojunctions of a large band gap and another with a smaller one [33]. TiO_2 can be used in a heterojunction with Cu_2O [34], CdS [35], PbS [36], g-C_3N_4 [37], Si [38] and with metals such as Au [39] or Ag [40,41], but ZnO has also been used in a heterojunction with CeO_2 [42], g-C_3N_4 [43], Ag [44], NiO [45] and BiOI [46] to name a few. Naturally, TiO_2 and ZnO composites were synthesised for photocatalytic purposes [47–49]. TiO_2 and ZnO containing inverse opal composites or sometimes called core-shell inverse opals in the literature were synthesised like TiO_2/WO_3 [50], ZnO/CuO [51], CuO_2/ZnO [52], Ag_3PO_4/ZnO [53], 3D TiO_2/-$BiVO_4$ [54], SiO_2/TiO_2 [55] FTO/TiO_2/$BiVO_4$ [56], 3D FTO/FTO/TiO_2 [57] and ZnO/TiO_2 [58–60] inverse opals. The TiO_2/ZnO and ZnO/TiO_2 bilayers are at the forefront of research; they can be used as layers on nanopillars [61], coating on graphitic-C_3N_4 [62], membrane coating [63], forming nanotubes [64], different nanocomposites [65] or antimicrobial layers [66].

TiO_2 ALD is a well-researched area due to the properties of ALD technique and TiO_2 based applications. An important aspect of thin films is their thickness and crystallinity; while the first depends on the cycle number of the ALD program, the latter depends on the deposition temperature and precursors. For typical $TiCl_4/H_2O$ deposition TiO_2 is amorphous at low temperatures (below 125–165 °C), then its anatase and at higher temperatures (350 °C) it is in rutile form. The thickness of the film has a direct effect on the roughness of the surface, which is also determined by the number of cycles and the deposition temperature [67]. Crystallinity has a large effect on photocatalysis, as crystals are favoured over amorphous structures. In the case of TiO_2, the anatase form is regarded superior [68]. Film thickness can affect photocatalysis due to the roughness of thin films, due to grain sizes, which have an optimal value at 150 nm [69] the case of ZnO, the case of crystallinity becomes easier, because the deposition of the amorphous ZnO layer is harder and more intentional. ZnO, even at room temperature, forms partially wurtzite thin films [70], and to grow amorphous films, the stoichiometry of ZnO must be shifted [71] or grown in ultrathin thickness [72]. Similarly to the number of cycles of TiO_2, the deposition temperature influences the film thickness, roughness of the surface and the grain size. A study has shown, that in the case of ZnO wurtzite thin films, film thickness of 50 nm and grain size of 20 nm are the optimum value [73]. To the knowledge of the authors, no article delves as deeply into the exact grain size and crystalline orientations depending on the ALD conditions during the deposition of bilayers. On the other hand, there are articles that optimized the bilayer structures to achieve maximum photocatalytic efficiency and comparisons were made to monolayers. 5 nm thick nanosheets of TiO_2, ZnO and TiO_2/ZnO were compared, where the bilayer performed tree times better [74]. In the cases of membrane coating, monolayers and bilayers in different ratios, were compared, and the 1:3 TiO_2:ZnO performed the best [75]. In the case of another membrane, the optimal bilayer cycle number ratio was found to be 80:40 TiO_2:ZnO and the optimal number of bilayers to be 7 [76]. Note, that in our case, the goal of the ALD deposition is the filling of the opal structure, which makes the layer thickness limited; however, the ratio of the two layers opens a new perspective for us to improve our results. Crystallinity was achieved during the heat treatment of the samples.

Substrates can influence photocatalytic efficiency. Usually, the substrate used in thin film growth influences the final properties of the layers, such as crystallinity (and crystal orientation), roughness and structural errors such as cracks [77–79]. Substrates can also affect the photocatalytic activity by different ways. As two examples: first, sodium from glass type substrates can diffuse into the TiO_2 layer and decrease the photocatalytic activity [80]; second, the substrate can have an effect on crystallization during heat treatment [81]. In our case, the purpose of the Si wafer is to be coated with the polystyrene opal sacrificial structure.

TiO_2 is a popular target material for photocatalytic applications, because of its chemical stability. ZnO has similar capabilities compared to TiO_2, but its photostability is lower, due to the dissolution of ZnO under UV light [82]. The application of a protective layer to ZnO to prevent its photocorrosion is a complex task, as the protective layer can decrease the photocatalytic activity of the coated photocatalyst [83]. Hence, there is a balance, between the two extremes: the bare ZnO photocatalyst, which is efficient, but prone to photocorrosion and the ZnO photocatalyst fully coated by a protective layer, which has lower efficiency, but is more stable. The intermediate state is a partially coated ZnO structure, which gives some protection, but still has significant photocatalytic activity [84]. Moreover, there are reports that the protective layer increased the photocatalytic activity, like a graphite-like layer on the ZnO particle [85]. The combination of ZnO and TiO_2 for this purpose is also evident, since TiO_2 is more stable. Ultrathin layers of TiO_2 were deposited on ZnO nanoparticles, which reduced the effect of photocorrosion and mainly preserved the photocatalytic efficiency of ZnO [86]. There are also cases in the literature as well in our work, where the TiO_2/ZnO and ZnO/TiO_2 composites proved to be less efficient photocatalysts, than ZnO or TiO_2. This can have multiple reasons: the additional deposition of the denser TiO_2 layer can decrease the number of particles per mass in the sample and this can be a misleading conclusion that the composite has a worse photocatalytic effect [87]. Similarly, an additional layer deposition can decrease the specific surface area of the samples [88]. Also, the annealing temperature can decrease the specific surface area and the number of active hydroxy groups on the surface of the material [89].

The purpose of this study is the preparation of TiO_2, ZnO, TiO_2/ZnO and ZnO/TiO_2 photocatalytically active, photonic inverse opals on Si substrates. Inverse opals are prepared, by coating opal crystals formed from vertically deposited polystyrene nanospheres with ZnO and TiO_2, and calcinating them at high temperature. Initial experiments on the effect of this high temperature (500 °C) calcination were performed on monolayers and bilayers. The characterisation of the layers and inverse opals was done by SEM, XRD, AFM, UV–Vis reflectance spectroscopy

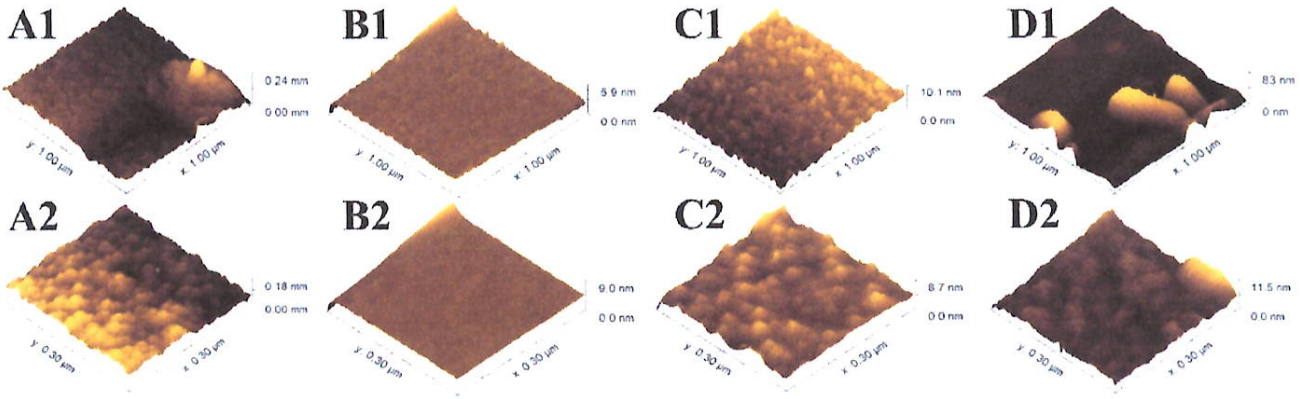

Fig. 1. AFM measurement of the metal-oxide layers. Image names: A – 36 nm ZnO, B – 36 nm TiO2, C – 18 nm ZnO/18 nm TiO2, D – 18 nm TiO2/18 nm ZnO and 1 – 1 × 1 μm, 2–0.3x0.3 μm.

and water contact angle measurement. Photocatalytic experiments were carried out using rhodamine 6G as the model molecule to decompose under UV and Vis irradiation.

2. Materials and methods

2.1. Preparation of the opal crystals

For the preparation, 460 nm diameter polystyrene nanospheres (Sigma Aldrich) were received in the form of a 10 w/w% water suspension, which was diluted to a 0.3 w/w% suspension and ultrasonicated for 2 h. Meanwhile, Si substrates were cut to make approximately 2 × 4 cm slides, these slides were cleaned with soap, then ethanol and distilled water, finally treated with a 'piranha' solution (3:1 mixture of concentrated sulfuric acid and 30 % hydrogen-peroxide) for 1 h. For vertical deposition, the slide was placed vertically in the suspension and got heat treated in a Nabertherm L9/11/B410 furnace with the following heat programme: 14 h at 50 °C, then 1,5 h at 80 °C. During vertical deposition, a large glass beaker filled with water was placed inside the furnace, as higher humidity in the furnace reduces the cracks of the opal crystal.

2.2. Atomic layer deposition

ZnO and TiO_2 depositions were carried out in a Beneq TFS-200-186 flow ALD reactor using DEZ (diethylzinc) for ZnO and $TiCl_4$ for TiO_2, water was used as co-reactant. The deposition was carried out at 50 °C and 1.4 mbar in the reactor and 7 mbar in the outer chamber, the pulse time was 300 ms and the purge time was 3 s for all samples. Four depositions were made, each time on an opal sample and an Si substrate: 36 nm ZnO by 434 cycles, 36 nm TiO_2 514 cycles, 18 nm ZnO by 217 cycles and 18 nm TiO_2 by 257 cycles and finally, 18 nm TiO_2 by 257 cycles and 18 nm ZnO by 217 cycles. The 36 nm layer thickness is equal to the smallest hole in an inverse opal made from 460 nm polystyrene nanospheres, this is due to the hexagonal structure of the opal. Layer thicknesses were calculated beforehand from preliminary deposited layers, which was checked using ellipsometry.

2.3. Inverse opal samples and layer annealing

Removal of the polystyrene nanospheres was done in the Nabertherm L9/11/B410 furnace. The coated opals were annealed with the following heat programme: the furnace was heated up to 500 °C under 4 h, then kept at this temperature for 2 h. The polystyrene nanospheres were removed from the inverse opal structure. The same heat treatment was applied to the monolayer and bilayer samples.

2.4. Characterization

The SEM images were taken to confirm the surface of the thin films in the micrometre scale and the structure of the inverse opals. For this we used a JEOL JSM 5500-LV scanning electron microscope, in high vacuum mode, and using the secondary electron detector. The samples were held in place with adhesive carbon tapes on top of the copper sample holder. For better image quality of the polystyrene and carbon opals, a layer of Au/Pd was sputtered on the samples.

EDX spectra were taken by the JEOL JSM-5500LV scanning electron microscope, for each sample three measurement points were averaged. This method can affirm the ALD deposition and is usually has a measuring depth of few μm.

XRD measurements of the inverse opal samples were made by a PANanalytical X'Pert Pro MPD X-ray diffractometer using Cu K-α radiation, between the angle range of 5°-65°. Crystallinity is an important factor in photocatalysis; determining it is crucial.

UV–Vis reflectance spectroscopy can reveal the optical structure of the samples, and this can indicate how these nanomaterials can act under light irradiation. This was measured by Avantes AvaSpec-2048 spectrophotometer equipped with optical cables; the substrate Si wafers were used as reference.

AFM measurements show the surface smoothness of the monolayer and bilayers on the nanometre scale. This was carried out by a Nanosurf C3000 atomic force microscope with a Tap190DLC needle in tapping mode.

Water contact angles were measured using a KRŰSS DSA30 drop shape analyser. This method can determine the polarity of thin film surfaces, this can affect the adsorption of dye molecules, which ultimately, determines the mechanism of photocatalysis. In addition, in the case of photocatalytic materials, the polarity of the surface increases as a result of irradiation, so the measurement of the contact angle can also provide information about the photocatalytic properties. Advancing contact angles were measured by the sessile drop method with ultrapure water (Adrona Integrity+, specific resistance: 18 MΩcm) at 22 °C and at least 80 % humidity. The data was recorded within the first minute after the 10 μL droplet formation. Receding contact angles were measured after removing 5 μL liquid from the droplet. Contact angle hysteresis was calculated as the difference of the advancing and receding angles. UV irradiations effect on the contact angles were explored using three-three stacked 18 W fluorescent lamps, facing each other at 10 cm distance. The samples were in the middle 5-5 cm away from the lamp stacks. The irradiation time was 2 h and the measurement points were at 0, 5, 10, 30, 60 and 120 min.

UV photocatalysis tests were carried out in a 30 ml 3,5x2,2 × 5 cm quartz cuvette with the inverse opal sample attached to one of the 3,5 × 5 cm sides. 10 ml of 5 × 10^{-5} mM rhodamin 6 G solution was poured

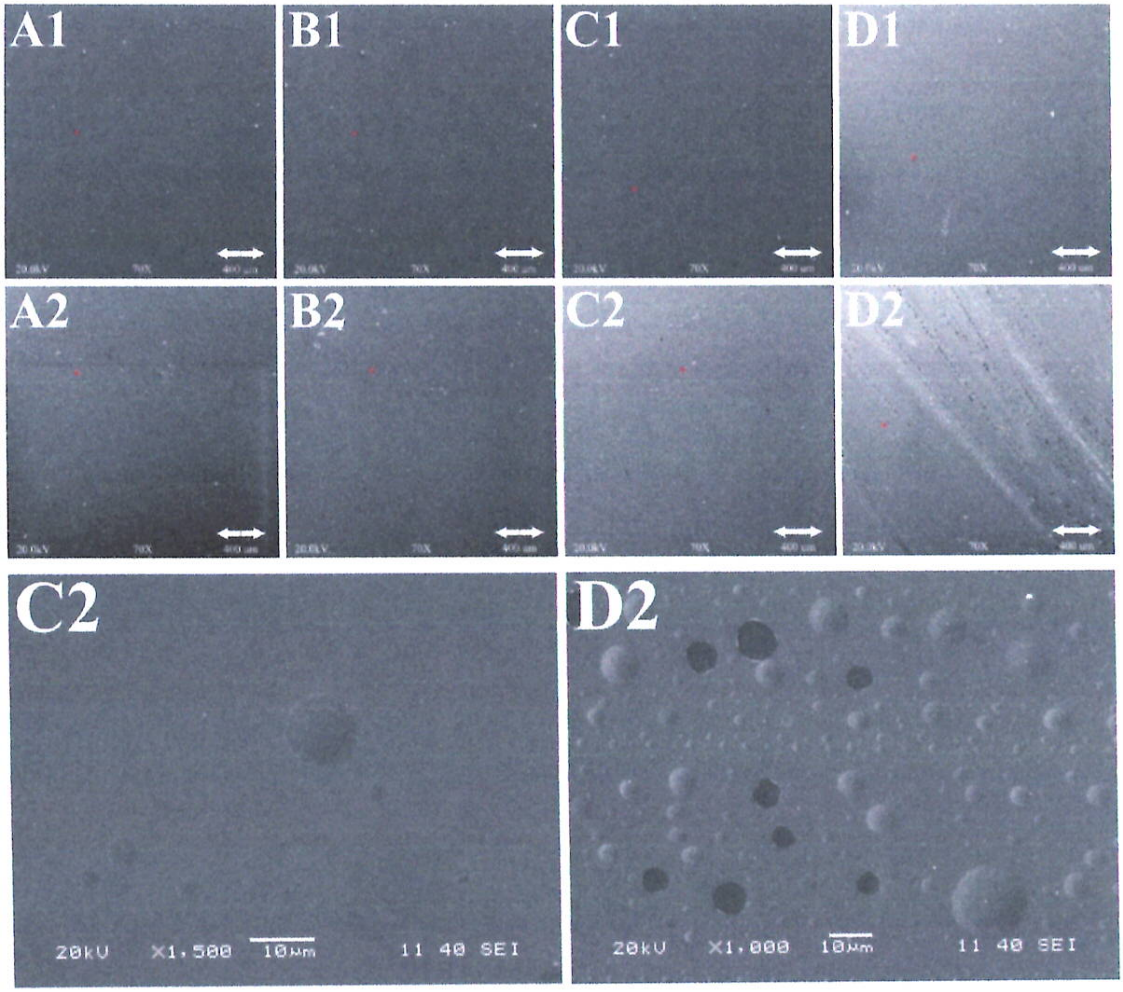

Fig. 2. SEM images of the mono- and bilayers. Samples name: A – 36 nm ZnO, B – 36 nm TiO2, C – 18 nm ZnO/18 nm TiO2, D – 18 nm TiO2/18 nm ZnO and 1 – before heat treatment, 2 – after heat treatment. Red crosses are the EDX measurement points.

into the cuvette, magnetic stirring was used and the top of the cuvettes was covered with parafilm to decrease the effect of evaporation. The geometry of the setup was the following: three-three 18 W fluorescent lamps, stacked were facing each other at 10 cm distance; the beforementioned cuvette was in the middle on top of a magnetic stirrer 5-5 cm away from the lamp stacks. The rhodamine 6 G solution with the sample was stirred for 15 min and then every half hour 3 mL of the solution was poured into a standard 1x1x4 cm cuvette for UV–Vis measurement for 4 h. For tests under visible light, the setup was the same.

Additional tests were performed on 4-nitrophenol under visible light irradiation with the set-up mentioned above, except for the concentration, which was $2.7*10^{-4}$ M and $1.9*10^{-4}$ M. 4-nitrophenol has a pK_A = 7.15 [90], this causes the nitrophenol spectra to change slightly during the photocatalysis test, so the pH was controlled between 10.0 and 10.5, which is also a beneficial environment for nitrophenol photodegradation [91]. The change in pH is a reported phenomenon for nitrophenol photocatalysis [92], because of this, pH adjustments were done by adding NaOH solution of pH = 14, this helped to avoid false positive measurement by dilution, because in each measurement step approximately 1 µL was added.

Table 1
Compositions of the ZnO and TiO_2 mono- and bilayers measured by EDX.

Before Heat Treatment	Mass%			
	Si	O	Zn	Ti
36 nm ZnO	93,16	4,31	2,54	–
36 nm TiO_2	95,18	3,94	–	0,89
18 nm ZnO/18 nm TiO_2	94,55	3,97	1,00	0,49
18 nm TiO_2/18 nm ZnO	94,51	4,24	0,92	0,34
After Heat Treatment	**Mass%**			
	Si	O	Zn	Ti
36 nm ZnO	93,11	3,91	2,99	–
36 nm TiO_2	95,09	3,80	–	1,11
18 nm ZnO/18 nm TiO_2	94,70	3,86	0,89	0,56
18 nm TiO_2/18 nm ZnO	94,71	3,61	1,17	0,51

3. Results and discussion

3.1. Mono- and bilayers

Before heat treatment, measurements with atomic force microscopy (Fig. 1.) were carried out on the samples with two different scanning area sizes (1 × 1 μm^2 and 0.3 × 0.3 μm^2). The 36 nm TiO_2 layer shows (Fig. 1/A1-2) a smooth surface compared to the other samples; this is since at 50 °C ALD deposition TiO_2 is amorphous [93]. According to the literature low temperature ALD deposition of ZnO provides a crystalline

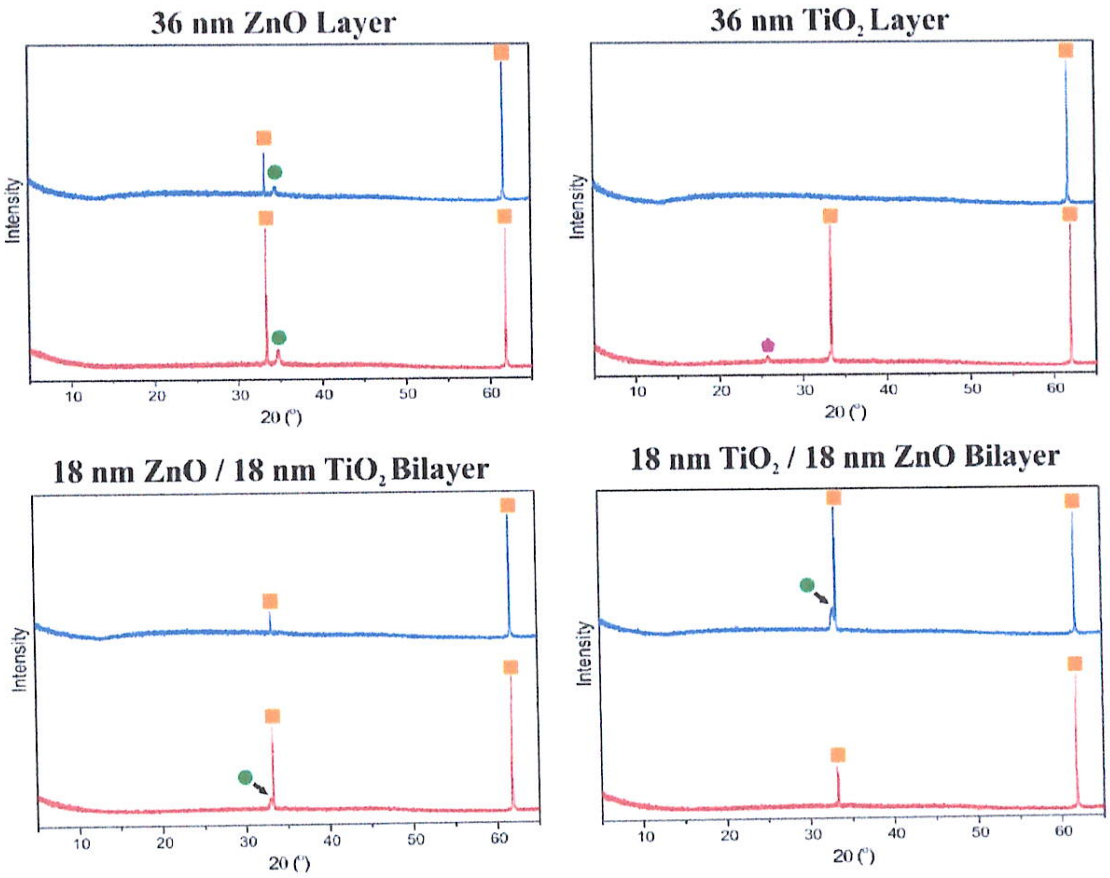

Fig. 3. X-ray diffractograms of the layers, before heat treatment and after heat treatment. ■Si substrate, ●ZnO layer, wurtzite and ●TiO_2 layer, anatase.

layer [73]. This may explain the visibly rugged surface of the samples containing a ZnO layer, which is possibly due to the crystalline grains of wurtzite.

Low magnification SEM images (Fig. 2.) show that the deposited layers are smooth at micrometre level for all samples. After heat treatment for the bilayer samples significant change can be observed (Fig. 2/C2-D2), for C2 black dots appear and for D2 black dots and white lines are visible to form a pattern. After further magnification (Fig. 2.), in the image of C2 humps, whereas in the image of D2 humps and holes can be observed. Similarly annealed ZnO and TiO_2 bilayers in the literature show that this process can cause cracks or other changes in the surface [94,95].

Energy dispersive X-ray analysis (EDX) measurements (Table 1) confirmed the presence of titanium and zinc in the films. The O content originates from the respective oxides and also from the native oxide layer on the Si substrate, the measuring depth of EDX can reach 1–2 μm, so this is expected. Interestingly, the mass of Zn was nearly double in the composite films compared to Ti, which was different from that expected from the ALD cycle numbers. This might be explained by the easier nucleation of ZnO than of TiO_2.

The crystallinity of the samples was explored by X-ray diffractometry, before and after heat treatment. The diffractograms of the ZnO and TiO_2 monolayer show (Fig. 3) that the ZnO layer deposited by ALD is crystalline both before and after heat treatment, while TiO_2 is initially amorphous but turns crystalline by annealing. The bilayers show a more interesting change. The diffractogram of the ZnO/TiO_2 bilayer initially shows a peak of ZnO wurtzite; after heat treatment, this disappears. Additionally, this ZnO peak has a different orientation [1 0 0] compared to the peak [0 0 2] of the ZnO monolayer. The TiO_2/ZnO layer shows that ZnO is crystalline, and the wurtzite peak disappears after heat treatment.

The optical properties of the samples were explored using UV–Vis reflectance spectroscopy. The ZnO monolayer has an observable peak (Fig. 4) around 300 and 363 nm, which shifts to around 290 and 380 nm after heat treatment. The absorption edge is also changing slightly. The TiO_2 monolayer has one peak around 410 nm; this shifts to 405 after the heat treatment. Interestingly, the optical properties of the bilayer change with heat treatment. Before heat treatment, the ZnO/TiO_2 bilayer spectra show two peaks (at 245 and 363 nm), the second peak is the same as the ZnO monolayer's. After heat treatment, the bilayer has one notable peak (at 407 nm), which is close to the 405 nm peak of the TiO_2 monolayer. The reverse tendency can be seen in spectra of the TiO_2/ZnO bilayer. Initially, before heat treatment, it has one large peak (at 403 nm), which is close to the 410 nm peak of the TiO_2 monolayer. After heat treatment, the TiO_2/ZnO peak shifts to the UV region (352 nm), and a second peak is observable around 245 nm).

Water contact angle measurements were taken to determine the wettability of the monolayers and bilayers. For each data point, four measurements were taken, and every measurement provided two contact angles (left and right sides of the droplet), so each advancing and receding contact angle was averaged out from eight contact angles. The monolayers and bilayers showed similar contact angles (Table 2) before heat treatment; the difference is within error. After heat treatment, the ZnO and the TiO_2/ZnO layers become more hydrophobic. In the case of the bilayer coating, this change can be attributed to the change in the crystalline structure of the ZnO layer on top (see Fig. 3), or the emerging

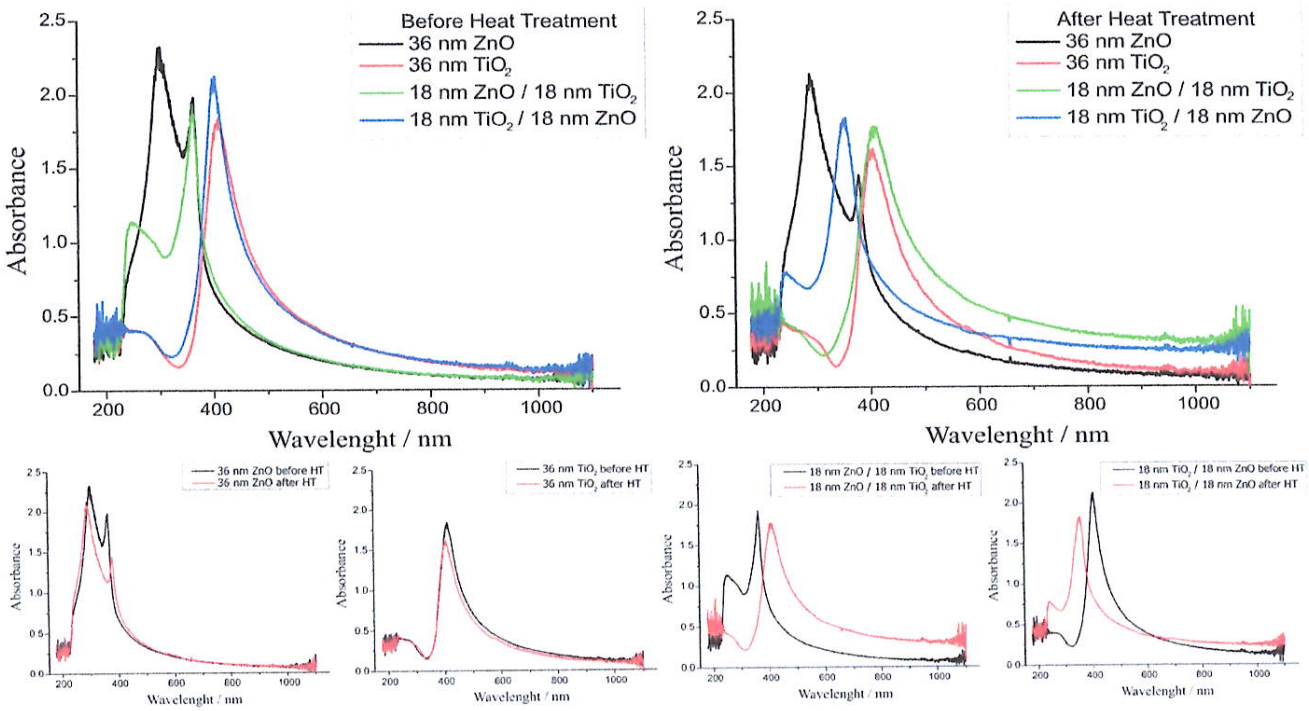

Fig. 4. UV–Vis reflectance spectrums of the mono- and bilayers. Large graphs present comparisons between the samples before and after the heat treatment (above), small graphs show the optical effect of the heat treatment (bottom).

Table 2
Results of the contact angle measurement.

Before Heat Treatment	Contact Angle		
	Advancing	Receding	Hysteresis
36 nm ZnO	77 ± 2	48 ± 2	31 ± 2
36 nm TiO_2	77 ± 2	47 ± 2	29 ± 2
18 nm ZnO/18 nm TiO_2	76 ± 3	47 ± 1	30 ± 3
18 nm TiO_2/18 nm ZnO	73 ± 1	39 ± 2	35 ± 2
After Heat Treatment	**Contact Angle**		
	Advancing	Receding	Hysteresis
36 nm ZnO	89 ± 1	50 ± 1	37 ± 2
36 nm TiO_2	62 ± 1	34 ± 1	28 ± 2
18 nm ZnO/18 nm TiO_2	75 ± 2	44 ± 1	31 ± 1
18 nm TiO_2/18 nm ZnO	83 ± 2	50 ± 1	32 ± 2

surface heterogeneities (Fig. 2, D2). As a result of the heat treatment, the surface became more polar in the case of the TiO2 monolayer, which may be related to the change in the crystal structure. In the case of the ZnO/TiO_2 layer, there is no change in the crystal structure of the upper layer, and the contact angles are also unchanged. The change of ZnO and TiO_2/ZnO changes can reflect to the EDX results (Table 1.), which showed that these layers lost significantly more oxygen during the heat treatment. The O vacancies could be the cause of the increased apolarity.

The changes in wettability of the samples were investigated under UV irradiation (see Fig. 5). The ZnO layer becomes more hydrophilic after long irradiation times. The thin TiO2 layer does not show a significant change in the contact angles. Zn/TiO_2 layer shows a decrease in contact angle after 20 min of irradiation and the TiO_2/ZnO layer remains around 80°. The contact angle of the Si substrate remains around 40.-50°.

3.2. Inverse opals

After the evaluation of the monolayers and bilayers the inverse opals were prepared by the same ALD programme on the sacrificial polystyrene opal templates. The template removal was done by the same programme as the heat treatment used on the mono and bilayers. Inverse opals were investigated by SEM, EDX, XRD and UV–Vis spectroscopy. Photocatalytic experiments were done under UV and visible light irradiation.

3.2.1. SEM images

SEM images (Fig. 6.) show the surface structure of the inverse opals. Images of the TiO_2 and the composite inverse opals show the remaining coating after the burn out of the opal crystal. The outline of the original nanospheres is visible. In the case of the ZnO inverse opal's surface, the inner hollow structure is visible, but it's covered. Interestingly, if this is due to the heat treatment process, it did not happen with the TiO_2/ZnO inverse opal.

3.2.2. EDX measurements

EDX measurements (Table 3.) of the samples show, that the ALD depositions were carried out successfully, which is indicated by the high amount of titan, zinc and oxygen. The high carbon presence might suggest that the annealing was not complete, this is more of an issue for the bilayered samples, but carbon could also be detected from the carbon tape used for the sample immobilisation for SEM. Silicon (substrate) levels also vary, between the monolayered and the two bilayered samples, this could indicate the difference in the inverse opal layer thickness, because the signal intensity can vary of the penetration depth of the electron beam. Al is detected from the SEM sample holder.

3.2.3. XRD diffractograms

XRD diffractograms (Fig. 7.) show, that all inverse opals proved to be crystalline, meaning that the initially deposited amorphous TiO_2 was annealed to anatase form. The most intense peaks are connected to the Si

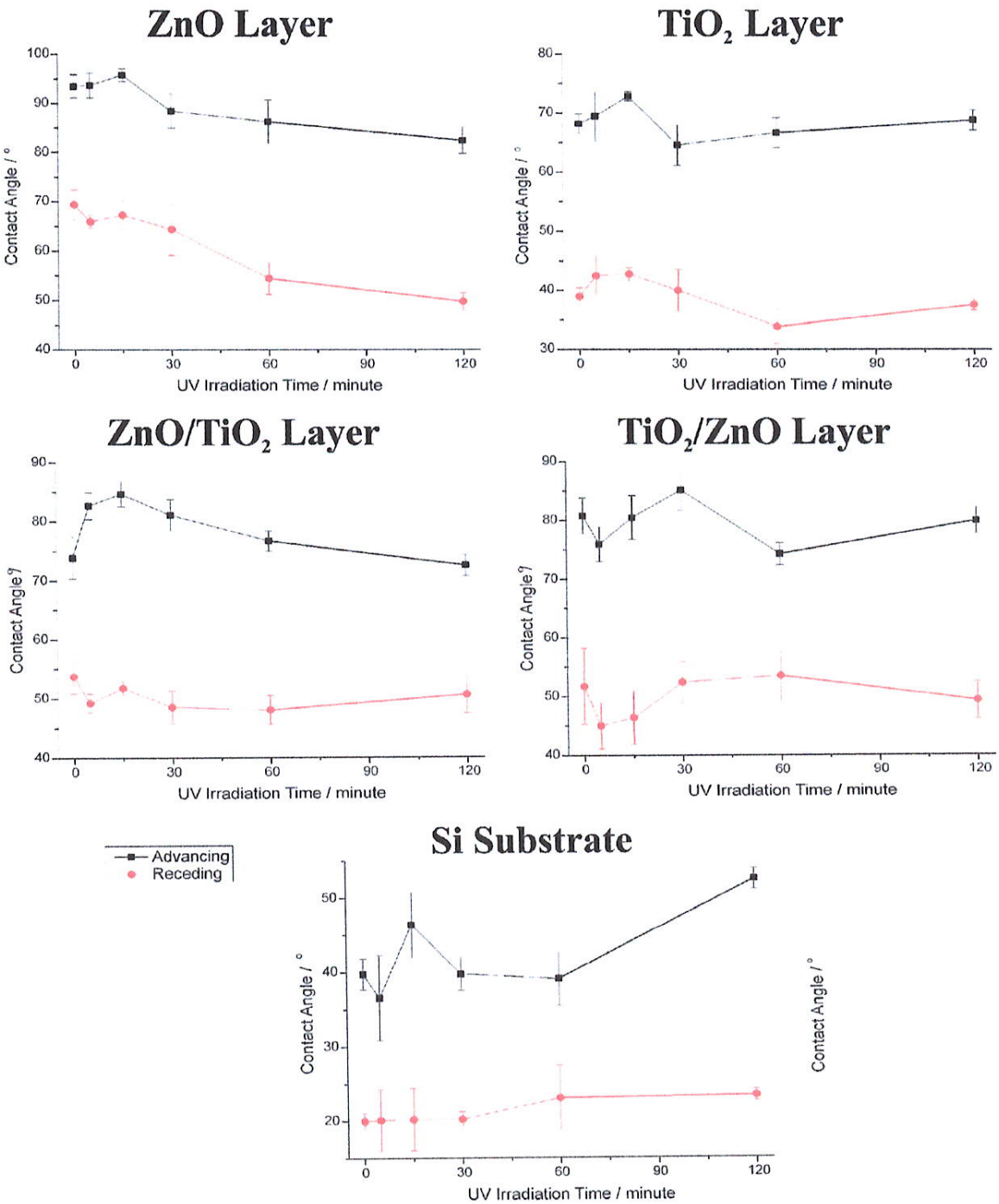

Fig. 5. Change of contact angles of layers under UV irradiation.

substrate. ZnO and TiO_2 inverse opals are in wurtzite and anatase form respectively. The composite inverse opals show the crystallinity of the top layer, for ZnO/TiO_2 its anatase and for TiO_2/ZnO its wurtzite.

3.2.4. UV–Vis spectroscopy

The UV–Vis spectra (Fig. 8.) of the inverse opals show the optical properties. The ZnO inverse opal has an absorption edge between 370 and 390 nm and an absorbance minimum, the photonic band gap around 600 nm. Normally, for ZnO thin films the UV–Vis spectra flatten after the adsorption edge [96], in this case individual peaks cannot be observed, but the increase in absorbance is induced by the 'slow' photon effect. The spectrum of the TiO_2 inverse opal is more complex, with an absorption edge starting from 230 nm, but it is hard to determine where it ends, because three peaks (375, 420 and 470 nm) overlap with it. A broad peak between 510 and 845 nm is observable. The absorption edge of the inverse ZnO/TiO2 opal is between 310 and 340 nm, has a small peak (365 nm) and a large broad peak between 430 and 750 nm. The TiO_2/ZnO inverse opal also has a more complex spectra, the absorption edge starts around 320 nm and is overlapping with a peak around 390 nm, it has a small peak at 450 nm, a broad peak between 475 and 720

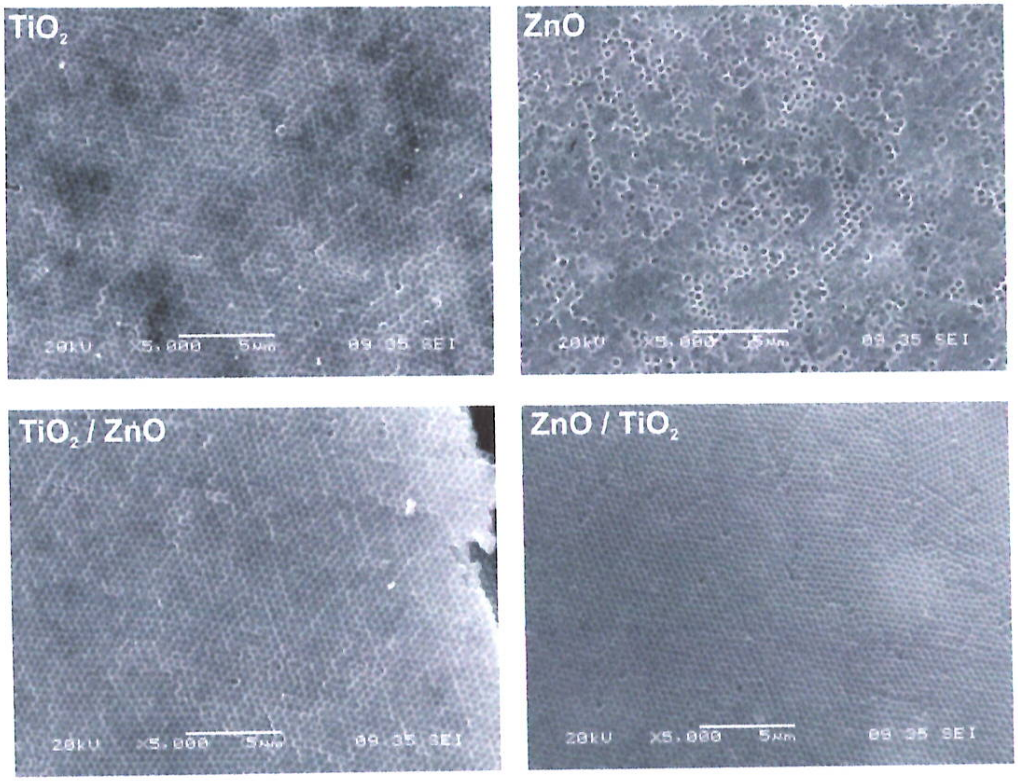

Fig. 6. SEM images of the inverse opal samples.

Table 3
Compositions of the ZnO and TiO_2 mono- and bilayered inverse opals measured by EDX.

Element/m/m%	TiO_2 IO	ZnO IO	TiO_2/ZnO IO	ZnO/TiO_2 IO
C	7.7	5.9	11.5	16.8
O	29.5	15.4	8.8	13.1
Al	0.5	1.4	5.7	2.0
Si	23.0	28.6	1.4	49.5
Cl	0.8	0.5	1.0	0.8
Ti	38.5	–	10.0	16.0
Zn	–	52.4	61.6	1.7

nm, and another small at 740 nm. The photonic band gap of the TiO_2, ZnO/TiO_2 and TiO_2/ZnO inverse opals is at 505 nm, 430 nm and 422 nm, respectively. The numerus number of peaks can be attributed to the 'slow' photon increased absorbance and the interference between the light reflected from the surface and the substrate.

Inverse opal samples show high hydrophilic characteristics with ZnO and the TiO_2/ZnO inverse opals showing sub 5° contact angles without irradiation. Interestingly, these two compositions showed increased contact angles after heat treatment, when it had a layer structure, this can indicate that inverse opal structure increases the hydrophilicity of these materials. TiO_2 inverse opal also reaches sub 5° contact angle after 2 h of UV irradiation and the ZnO/TiO_2 composite inverse opal also reaches sub 10° contact angle (Fig. 9).

Inverse opal samples show high hydrophilic characteristics, ZnO and the TiO_2/ZnO inverse opals showed sub 5° contact angles, moreover TiO_2 inverse opal also reached sub 5° after 2 h of UV irradiation and ZnO/TiO_2 reached around 10°.

3.2.5. Photocatalytic experiments

Photocatalysis experiments using UV lamps (Fig. 10 and 11.) showed that the inverse opal samples are capable of decomposing rhodamine 6G. The efficiency in order is TiO_2/ZnO (the best), TiO_2, ZnO and ZnO/TiO_2, these inverse opals decomposed 41 %, 34 % 18 % and 11 % of the rhodamine 6G during the investigated time of irradiation. TiO_2/ZnO inverse opal performed the best, on the other hand the ZnO/TiO_2 has the poorest performance. The substrate decomposed 6 % of rhodamine 6G. Difference between the TiO_2/ZnO and the ZnO/TiO_2 could be understood by the difference in wettability, which is observable in the UV irradiation contact angle measurements.

Serial experiments were performed with the two bilayer samples under UV light. The efficiency reduction was on the scale of 1–2%, in the case of the TiO_2/ZnO inverse opal the final degradations were 66 %, 68 % and 71 % and for the ZnO/TiO_2 it is 91 %, 93 % and 93 %. The difference between the two systems is that TiO_2 is more resistant to photocorrosion and is used for ZnO as a protective layer in the literature [97].

Visible light-induced photocatalysis experiments differed in the activity of the inverse opals. Bilayered inverse opals proved to be the most efficient samples by decomposing 14 % and 11 % of rhodamine 6G during the invstigated time of irradiation. The ZnO inverse opal is also close with 9 % and the last is TiO_2 inverse opal with 7 %, which is close to the blank and substrate's performance, this shows, that non-composite TiO_2 inverse opal is inefficient under visible light irradiation. It is observable, that under visible light, the composite inverse opals perform better, this could be because under visible light charge separation has a more dominant effect on photocatalysis.

Interestingly, in both cases the TiO_2/ZnO had the highest efficiency, on the other hand, while the ZnO/TiO_2 was the worst under UV light, it proved to be better under visible light irradiation than the monolayered inverse opals. It is also observable, that TiO_2 inverse opal performs better under UV, but becomes practically unusable under visible light, at the same time, ZnO inverse opal becomes better under visible light. It is also notable, that the bilayer works better, if the inner layer is TiO_2 and the outer layer is the ZnO (see Figs. 12–14).

The initial concentration of Rhodamin 6 G and pH was tested on the

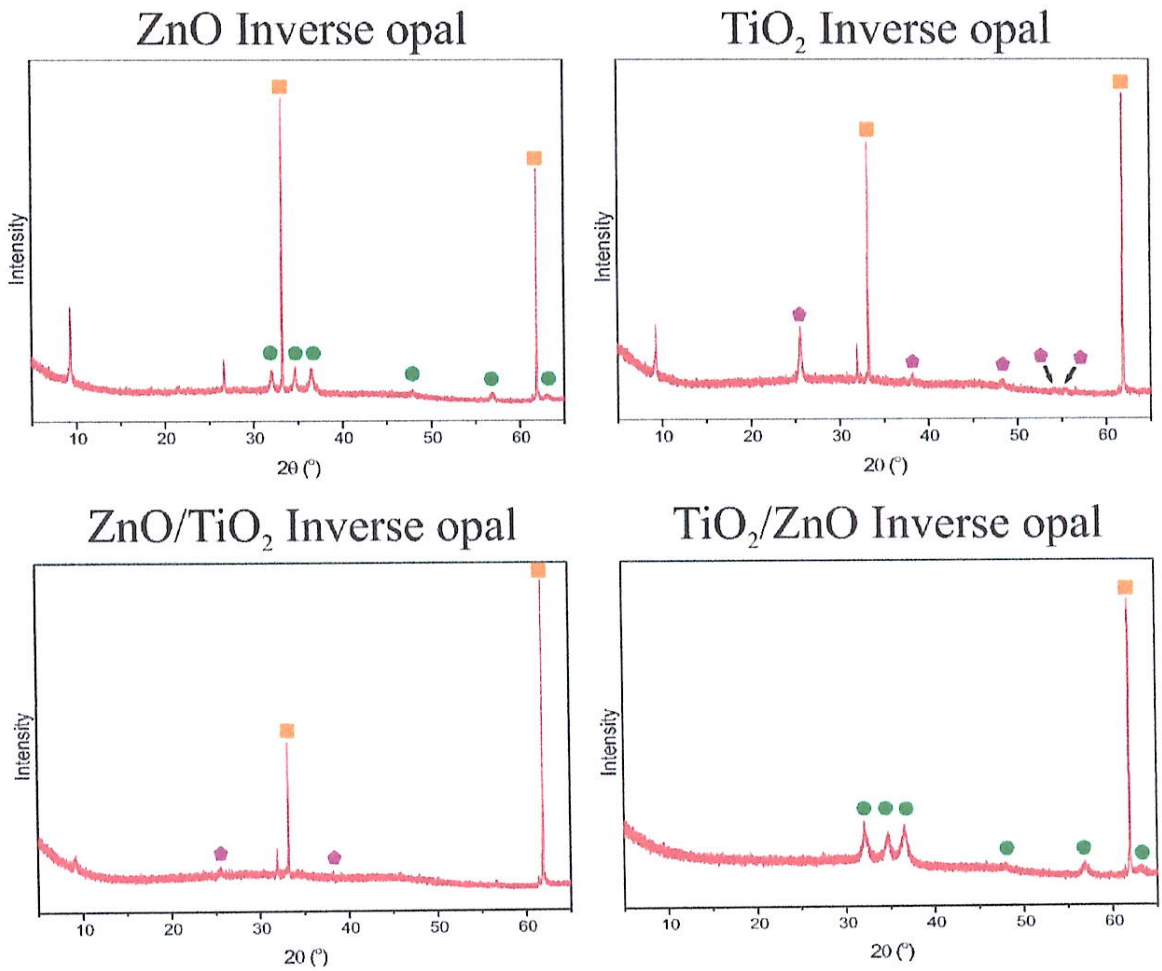

Fig. 7. X-ray diffractograms of inverse opals. Si substrate, ZnO layer, wurtzite and TiO_2 layer, anatase.

photocatalytic efficiency of the bilayered inverse opals. Changing the initial concentration from $1.5*10^{-5}$ decreased the activity of the TiO_2/ZnO inverse opal. In the case of the ZnO/TiO_2 inverse opal, reducing it to $0.93*10^{-5}$ improved the degradation rate. The initial pH had the same effect to both bilayered inverse opals; more acidic environment decreased the efficiency of photocatalysis, but the more basic pH improved it. These findings are mainly consistent with the literature [98].

An experiment closer to life with an organic pollutant other than Rhodamine 6 G was tested on the best bilayer; the TiO_2/ZnO inverse opal. Now, our choice was nitrophenol, which is also used as a model pollutant and is harder to decompose. The pH of the nitrophenol was kept between pH 10.0–10.5, method is described in Chapter 2.4 Characterization. In some articles, it is usually photocatalyzed using a reduction agent like sodium-borohydride [99] or hydrogen-peroxide [100]. However, we measured a 10 % degradation of nitrophenol, without using reducing agents; on the other hand, the pH was in a favourable basic environment.

4. Outlook

Inverse opal photocatalysis still faces two big problems; one is the scalability and environmental friendliness of the production process and some aspects of the usability.

The production method of this material can be divided into the main steps of synthesis of the raw materials (polystyrene nanospheres and precursors vertical deposition, layer deposition and heat treatment. Polymer nanosphere production is viable via the emulsion polymerization mechanism [101], which is an applicable method on an industrial scale [102]. Vertical deposition was our choice of method for the preparation of opal crystals, since it is relatively easy and economical. The main problem is not the upward scaling of the method, it is possible to coat larger surfaces [103,104], but the time. Faster methods based on the principles of vertical deposition usually use another force or mechanism to speed up the process, this can be imbibition [105], electric force [106], magnetic force [107], or reduced pressure [108]. ALD precursors are usually organometallic compounds, which are widely used in industrial synthesis as a methylation reagent [109]. Historically, the first industrial use of ALD was the coating of thin film electroluminescence (TFEL) displays, but it became more widely known after its application in the electronics industry [110]. Nowadays, there are studies for the use of ALD in solar panels [111] and astronomical mirrors [112], these substrates demand a larger reactor chamber, which can be on meter scale [112]. Another methodology is the roll-to-roll ALD technique, which utilizes a conveyor system to continuously deposit, this technically can coat "infinitely", very long substrates [113,114].

Environmentally friendly materials are the focal point of research nowadays, such as photocatalysis. However, it is questionable whether the production or degradation of a photocatalyst has serious impact on the environment, whether it is worth producing. In our case, the source

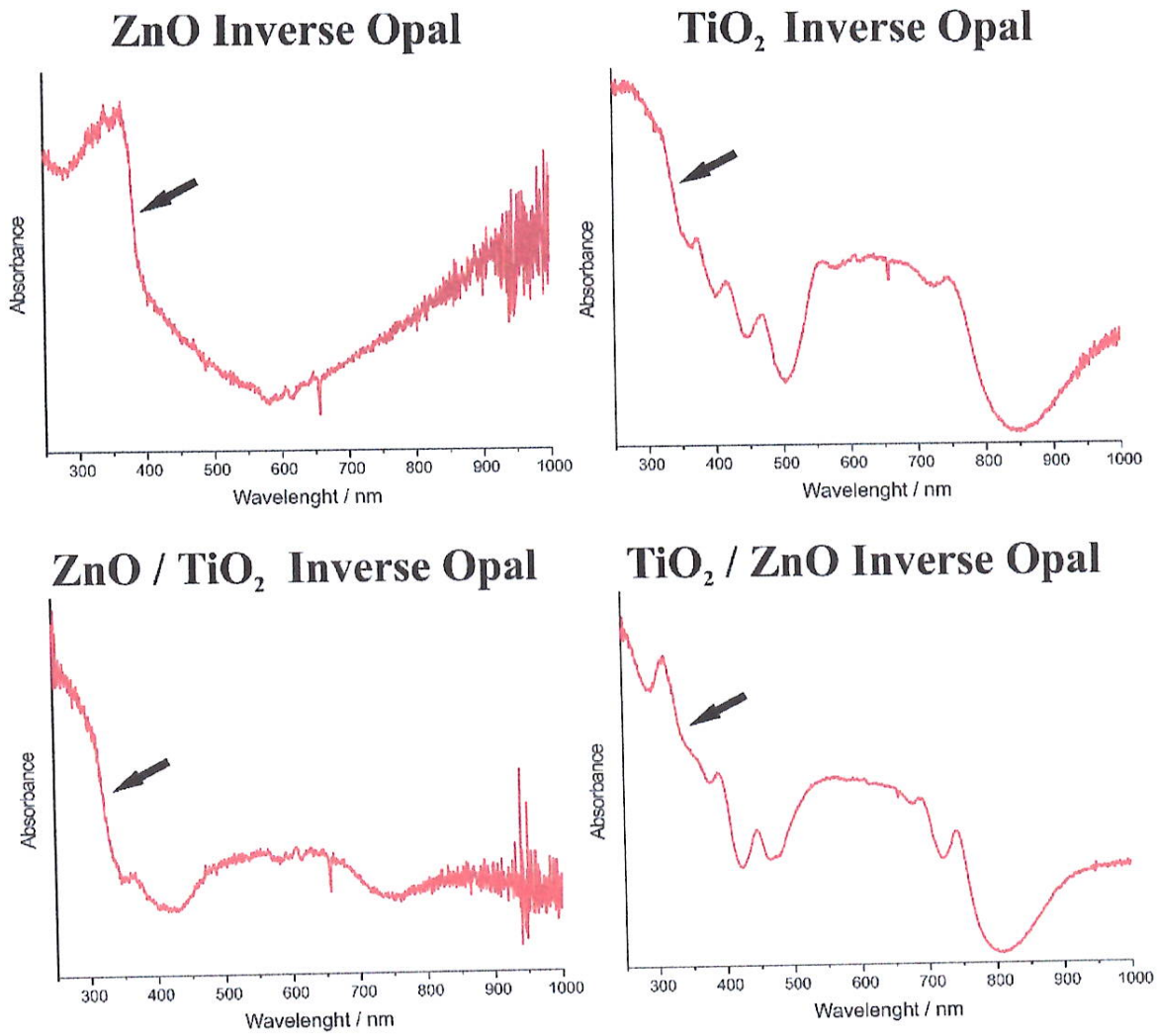

Fig. 8. UV–Vis reflectance spectra of the layer. Above large graphs present comparisons between the sample before and after the heat treatment, bottom small graphs show the optical effect of the heat treatment. ➡ Absorption edge.

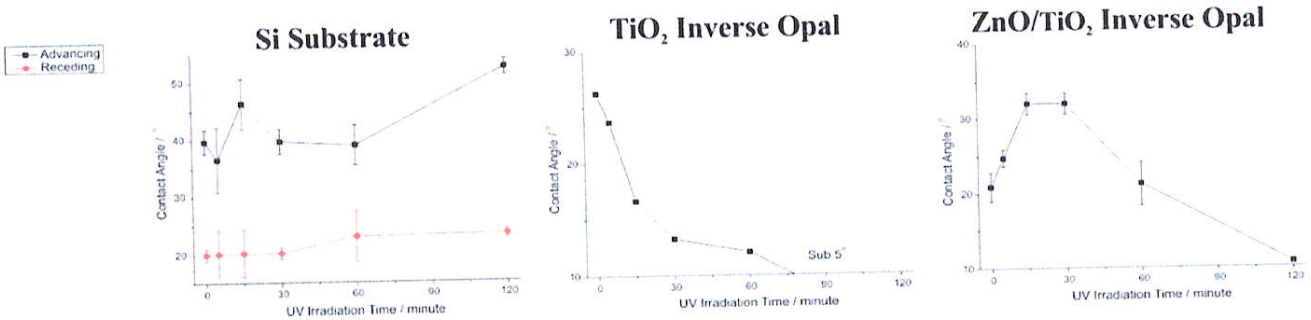

Fig. 9. Change of contact angles under UV irradiation of the inverse opals (substrate for reference). ZnO inverse opal and TiO_2/ZnO inverse opal contact angles were sub 5° without UV irradiation.

of danger to the environment can come from the synthesis and degradation of the catalyst. The synthesis uses polystyrene nanoparticles, which have a tremendous literature to be hazardous to living organisms [115,116]. This problem can be solved by preventing polystyrene from being released into the environment through the manufacturing process, or by replacing it with more environmentally friendly or degradable nanospheres [117] through an environmentally friendly synthesis path [118]. Atomic layer deposition has several major problems with respect to its impact on the environment; the precursors (mainly, its synthesis), the temperature and working duration (energy consumption) and the inefficient use of the precursors [119]. The development to solve these issues is underway; to name a few examples, the duration of the ALD deposition can be reduced by the spatial ALD method [119] or green chemistry can be applied for precursor synthesis [120]. A catalyst can

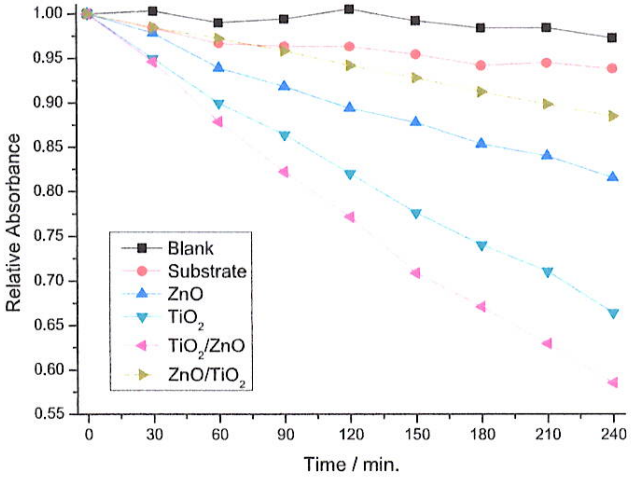

Fig. 10. Photocatalytic degradation monitored by UV–Vis spectroscopy for the inverse opal samples under UV light irradiation.

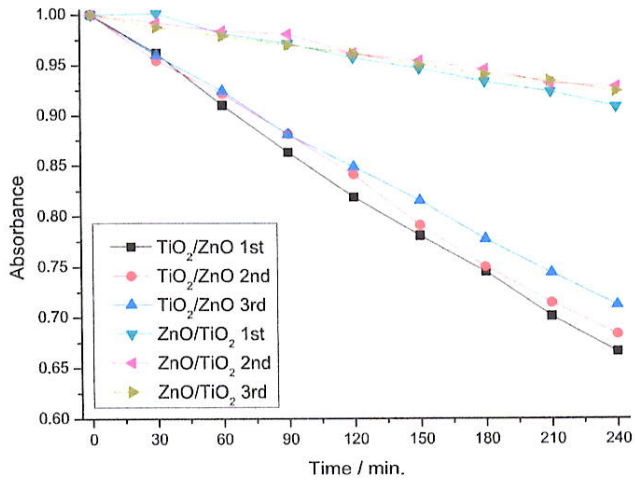

Fig. 11. Stability experiments of the bilayered inverse opal samples under UV light.

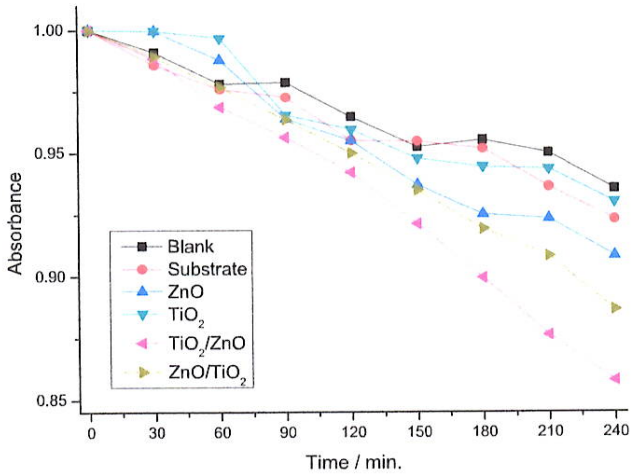

Fig. 12. Photocatalytic degradation monitored by UV–Vis spectroscopy for the inverse opal samples under visible light irradiation.

impact the environment in two ways; it can mechanically break and get into nature, or photocorrosion can degrade it. The first case is solvable using filters, but the second is trickier; since Zn^{2+} or Ti^{4+} can enter the environment [121,122]. This is mainly a problem for ZnO-based catalysis, because TiO_2 is much more stable. Photocorrosion is preventable by modification of crystallinity, doping, use of a cocatalyst, composite with carbon nanomaterial, heterojunctions and control over reaction parameters [123].

5. Conclusion

5.1. Layer structures

Mono- and bilayers were deposited using ALD on silica substrates to study the effects of the 500 °C heat treatment process of sacrificial template removal and crystallization. AFM measurements show the precision of the ALD technique and the contrast between the amorphous TiO_2 and wurtzite ZnO. SEM images show, that the heat treatment creates humps and holes on the surface of the bilayers due to the high temperature or crystallization, later is supported by the XRD. UV–Vis spectroscopy proves, that the heat treatment has little effect on monolayers, in contrast the ZnO/TiO_2 bilayer's spectra redshifted and the TiO_2/ZnO bilayer's spectra blueshifted. Heat treatment had an effect on wettability, ZnO became less hydrophilic and TiO_2 became more hydrophilic. In the case of the bilayers, the ZnO/TiO_2 wettability did not change, but the TiO_2/ZnO became less hydrophilic like the ZnO monolayer, this could be explained by O vacancies as the EDX data shows lower O amount.

5.2. Inverse opal structure

The preparation of the TiO_2, ZnO and composite inverse opals were successfully prepared using vertical deposition and ALD, which is proved by SEM and EDX. XRD diffractograms indicate the crystallinity of the materials, which are anatase for TiO_2 and wurtzite for ZnO. Optical properties were explored using UV–Vis reflectance spectroscopy, which shows a simple optical structure for the ZnO inverse opal, but a more complex one for the TiO_2 and the bilayered inverse opals. Photocatalysis experiments using UV irradiation showed, that the most effective TiO_2/ZnO inverse opal due to its lower contact angle, hence better wettability. TiO_2 performs better than ZnO in contract to its worse wettability, however ZnO has more O vacancies showed by EDX in the reference layers. Under visible light irradiation, photocatalysis tests showed that TiO_2/ZnO inverse opal still performs the best, but the ZnO/TiO_2 is also comparable and the TiO_2 and ZnO inverse opals efficiency is close to the substrates. This might indicate that under visible light, apart from the "slow" photon effect, charge separation plays a dominant role in photocatalysis. Additionally, measurements were done for the further optimization of the catalysis systems by setting optimal pH and concentration. The best performing catalyst, the TiO_2/ZnO inverse opal is capable of degrade 4-nitrophenol at alkaline pH without reducing agents using visible light irradiation.

CRediT authorship contribution statement

Dániel Attila Karajz: Validation, Supervision, Methodology, Investigation, Formal analysis, Data curation, Conceptualization. **Csenge Anna Fónay:** Investigation, Formal analysis. **Bence Parditka:** Methodology, Investigation. **Zoltán Erdélyi:** Methodology, Investigation, Funding acquisition. **Péter Márton:** Methodology, Investigation, Formal analysis. **Zoltán Hórvölgyi:** Validation, Methodology, Investigation. **Imre Miklós Szilágyi:** Validation, Supervision, Funding acquisition.

Declaration of competing interest

No conflict of interest.

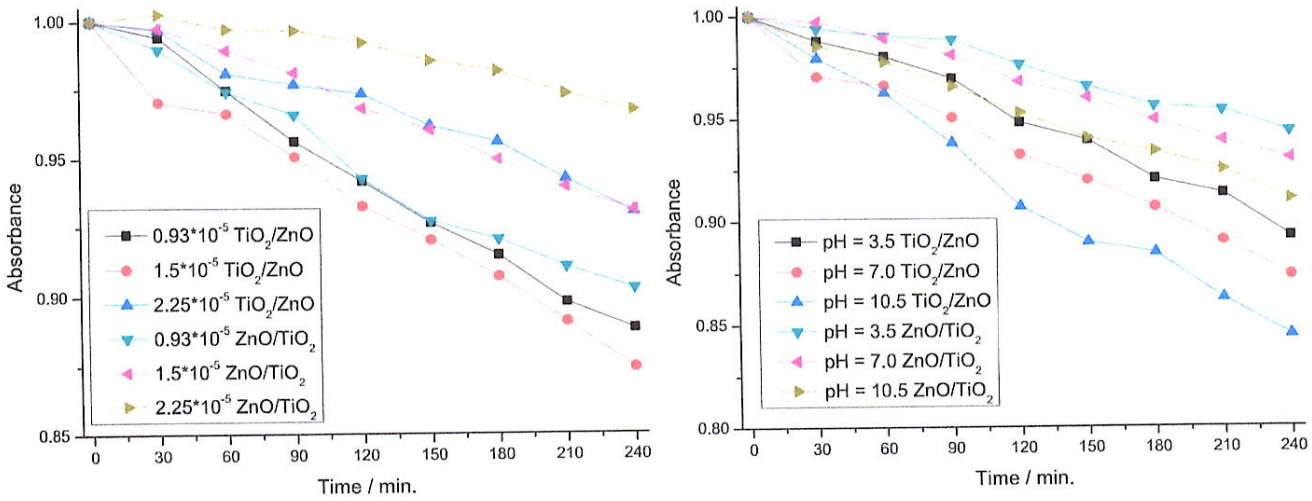

Fig. 13. Initial pollutant concentration (left) and pH (right) effect on the photocatalytic efficiency.

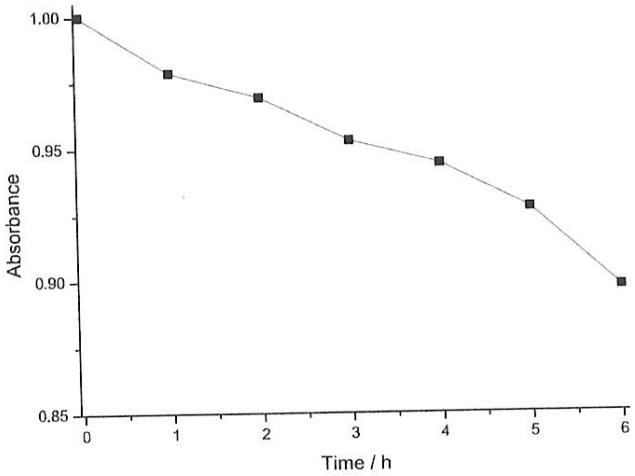

Fig. 14. Photocatalytic degradation of 4-nitrophenol under visible light irradiation, pH = 10.0–10.5.

Data availability

No data was used for the research described in the article.

Acknowledgements

This research is part of projects no. TKP2021-NVA-02 and TKP2021-EGA-02, which have been implemented with the support provided by the Ministry of Culture and Innovation of Hungary from the National Research, Development and Innovation. Fund, financed under the TKP2021-NVA and TKP2021-EGA funding scheme. Project no. TKP2021-NKTA-34 has been implemented with the support provided from the National Research, Development and Innovation Fund of Hungary, financed under the TKP2021-NKTA funding scheme. Supported by the University of Debrecen Program for Scientific Publication.

References

[1] J.I.L. Chen, G. von Freymann, S.Y. Choi, V. Kitaev, G.A. Ozin, Slow photons in the fast lane in chemistry, J Mater Chem [Internet] 18 (2008) 369–373. Available from: http://xlink.rsc.org/?DOI=B708474A.

[2] Y. Nishijima, K. Ueno, S. Juodkazis, V. Mizeikis, H. Misawa, T. Tanimura, et al., Inverse silica opal photonic crystals for optical sensing applications, Opt Express 15 (2007).

[3] D. McNulty, H. Geaney, E. Armstrong, C. O'Dwyer, High performance inverse opal Li-ion battery with paired intercalation and conversion mode electrodes, J Mater Chem A Mater (2016).

[4] X. Zhang, S. John, Enhanced photocatalysis by light-trapping optimization in inverse opals, J Mater Chem A Mater 8 (2020) 18974–18986.

[5] C.E. Creissen, J. Warnan, D. Antón-García, Y. Farre, F. Odobel, E. Reisner, Inverse opal CuCrO2 photocathodes for H2 production using organic dyes and a molecular Ni catalyst, ACS Catal. 9 (2019).

[6] M. Deimling, S.R. Kousik, K. Abitaev, W. Frey, T. Sottmann, K. Koynov, et al., Hierarchical silica inverse opals as a catalyst support for asymmetric molecular heterogeneous catalysis with chiral Rh-diene complexes, ChemCatChem 13 (2021).

[7] G.I.N. Waterhouse, J.B. Metson, H. Idriss, D. Sun-Waterhouse, Physical and optical properties of inverse opal CeO2 photonic crystals, Chem. Mater. 20 (2008).

[8] G.J. McIntosh, J.B. Metson, Surface area characteristics of furfuryl-alcohol-derived inverse opal carbons produced from silica inverse opal templates, J. Mater. Sci. 51 (2016).

[9] Y.A. Vlasov, X.Z. Bo, J.C. Sturm, D.J. Norris, On-chip natural assembly of silicon photonic bandgap crystals, Nature 414 (2001) 289–293.

[10] J. Liu, J. Jin, Y. Li, H.W. Huang, C. Wang, M. Wu, et al., Tracing the slow photon effect in a ZnO inverse opal film for photocatalytic activity enhancement, J Mater Chem A Mater 2 (2014).

[11] H. Xiang, S. Yang, E. Talukder, C. Huang, K. Chen, Research and application progress of inverse opal photonic crystals in photocatalysis, Inorganics (Basel) (2023).

[12] G.I.N. Waterhouse, M.R. Waterland, Opal and inverse opal photonic crystals: fabrication and characterization, Polyhedron 26 (2007) 356–368.

[13] E. Yablonovitch, Photonic band-gap structures, Journal of the Optical Society of America B [Internet] 10 (1993) 283. Available from: https://www.osapublishing.org/abstract.cfm?URI=josab-10-2-283.

[14] M. Curti, G. Zvitco, M.A. Grela, C.B. Mendive, Angle dependence in slow photon photocatalysis using TiO2 inverse opals, Chem. Phys. 502 (2018).

[15] X. Feng, K. Kang, Y. Wu, J. Zhang, L. Wang, Exploring the slow-light effect of Pt/TiO2-SiO2inverse opal on photocatalytic nonoxidative coupling of methane, Chem. Commun. 57 (2021).

[16] T. Mackawa, Y.S. Huang, N. Tateishi, A. Nakanishi, T. Onoe, Y. Dong, et al., Slow photon photocatalytic enhancement of H2 production in TaON inverse opal photonic crystals, J. Solid State Chem. 329 (2024).

[17] J. Low, L. Zhang, B. Zhu, Z. Liu, J. Yu, TiO2 photonic crystals with localized surface photothermal effect and enhanced photocatalytic CO2 reduction activity, ACS Sustain Chem Eng 6 (2018).

[18] J. Yu, J. Lei, L. Wang, J. Zhang, Y. Liu, TiO2 inverse opal photonic crystals: synthesis, modification, and applications - a review, J. Alloys Compd. (2018) 740–757.

[19] S. Meng, D. Li, P. Wang, X. Zheng, J. Wang, J. Chen, et al., Probing photonic effect on photocatalytic degradation of dyes based on 3D inverse opal ZnO photonic crystal, RSC Adv. 3 (2013).

[20] J. Wang, Y. Wan, X. Wang, Y. Pu, N. Ali, S. Yuan, et al., Fabrication and characterization of inverse opal tin dioxide as a novel and high-performance photocatalyst for degradation of Rhodamine B dye, Inorganic and Nano-Metal Chemistry 51 (2021).

[21] J.K. Kim, J.H. Moon, T.W. Lee, J.H. Park, Inverse opal tungsten trioxide films with mesoporous skeletons: synthesis and photoelectrochemical responses, Chem. Commun. 48 (2012).

[22] L. Zhang, C. Baumanis, L. Robben, T. Kandiel, D. Bahnemann, Bi 2WO 6 inverse opals: facile fabrication and efficient visible-light-driven photocatalytic and photoelectrochemical water-splitting activity, Small 7 (2011).

[23] H. Kisch, Semiconductor photocatalysis: principles and applications. Semiconductor Photocatalysis: Principles and Applications, 2015.

[24] U. Rafiq, K. Majid, Mitigating the charge recombination by the targeted synthesis of Ag2WO4/Bi2Fe4O9 composite: the facile union of orthorhombic semiconductors towards efficient photocatalysis, J. Alloys Compd. 842 (2020).

[25] I. Ahmad, M. Muneer, A.S. Khder, S.A. Ahmed, Novel type-II heterojunction binary composite (CdS/AgI) with outstanding visible light-driven photocatalytic performances toward methyl orange and tetracycline hydrochloride, ACS Omega 8 (2023).

[26] K. Siwińska-Stefańska, A. Kubiak, A. Piasecki, A. Dobrowolska, K. Czaczyk, M. Motylenko, et al., Hydrothermal synthesis of multifunctional TiO 2 -ZnO oxide systems with desired antibacterial and photocatalytic properties, Appl. Surf. Sci. 463 (2019).

[27] D. Barreca, E. Comini, A.P. Ferrucci, A. Gasparotto, C. Maccato, C. Maragno, et al., First example of ZnO-TiO2 nanocomposites by chemical vapor deposition: structure, morphology, composition, and gas sensing performances, Chem. Mater. 19 (2007).

[28] L. Lin, Y. Yang, L. Men, X. Wang, D. He, Y. Chai, et al., A highly efficient TiO2@ZnO n-p-n heterojunction nanorod photocatalyst, Nanoscale 5 (2013).

[29] N. Bai, X. Liu, Z. Li, X. Ke, K. Zhang, Q. Wu, High-efficiency TiO2/ZnO nanocomposites photocatalysts by sol-gel and hydrothermal methods, J. Sol. Gel Sci. Technol. 99 (2021).

[30] R. Asahi, T. Morikawa, T. Ohwaki, K. Aoki, Y. Taga, Visible-light photocatalysis in nitrogen-doped titanium oxides, Science 293 (2001) 269–271, 1979.

[31] K. Choi, T. Kang, S.G. Oh, Preparation of disk shaped ZnO particles using surfactant and their PL properties, Mater. Lett. 75 (2012).

[32] C. Dette, M.A. Pérez-Osorio, C.S. Kley, P. Punke, C.E. Patrick, P. Jacobson, et al., TiO2 anatase with a bandgap in the visible region, Nano Lett. 14 (2014).

[33] Y. Wang, J. Yu, W. Peng, J. Tian, C. Yang, Novel multilayer TiO2 heterojunction decorated by low g-C3N4 content and its enhanced photocatalytic activity under UV, visible and solar light irradiation, Sci. Rep. 9 (2019).

[34] M. Tavakolian, K. Keshavarz, M. Hosseini-Sarvari, Cu2O/TiO2 as a sustainable and recyclable photocatalyst for gram-scale synthesis of phenols in water, Mol. Catal. 514 (2021).

[35] A. Kaur, A. Umar, W.A. Anderson, S.K. Kansal, Facile synthesis of CdS/TiO2 nanocomposite and their catalytic activity for ofloxacin degradation under visible illumination, J. Photochem. Photobiol. Chem. 360 (2018).

[36] S.B. Bubenhofer, C.M. Schumacher, F.M. Koehler, N.A. Luechinger, R.N. Grass, W. J. Stark, Large-scale synthesis of PbS-TiO 2 heterojunction nanoparticles in a single step for solar cell application, J. Phys. Chem. C 116 (2012).

[37] M.A. Alcudia-Ramos, M.O. Fuentez-Torres, F. Ortiz-Chi, C.G. Espinosa-Gonzalez, N. Hernandez-Como, D.S. García-Zaleta, et al., Fabrication of g-C3N4/TiO2 heterojunction composite for enhanced photocatalytic hydrogen production, Ceram. Int. 46 (2020).

[38] G. Sahasrabudhe, S.M. Rupich, J. Jhaveri, A.H. Berg, K.A. Nagamatsu, G. Man, et al., Low-temperature synthesis of a TiO2/Si heterojunction, J. Am. Chem. Soc. 137 (2015).

[39] L.A. Al-Hajji, A.A. Ismail, A. Bumajdad, M. Alsaidi, S.A. Ahmed, F. Almutawa, et al., Construction of Au/TiO2 Heterojunction with high photocatalytic performances under UVA illumination, Ceram. Int. 46 (2020).

[40] L. Barrientos, P. Allende, M.A. Laguna-Bercero, J. Pastrian, J. Rodriguez-Becerra, L. Caceres-Jensen, Controlled Ag-TiO2 heterojunction obtained by combining physical vapor deposition and bifunctional surface modifiers, J. Phys. Chem. Solid. 119 (2018).

[41] B. Tegze, E. Albert, B. Dikó, N. Nagy, A. Rácz, G. Sáfrán, et al., Effect of silver modification on the photoactivity of titania coatings with different pore structures, Nanomaterials 11 (2021).

[42] E. Cerrato, C. Gionco, M.C. Paganini, E. Giamello, E. Albanese, G. Pacchioni, Origin of visible light photoactivity of the CeO2/ZnO heterojunction, ACS Appl. Energy Mater. 1 (2018).

[43] W. Yu, D. Xu, T. Peng, Enhanced photocatalytic activity of g-C3N4 for selective CO2 reduction to CH3OH via facile coupling of ZnO: a direct Z-scheme mechanism, J Mater Chem A Mater 3 (2015).

[44] D. Lin, H. Wu, R. Zhang, W. Pan, Enhanced photocatalysis of electrospun Ag-ZnO heterostructured nanofibers, Chem. Mater. 21 (2009).

[45] Z. Zhang, C. Shao, X. Li, C. Wang, M. Zhang, Y. Liu, Electrospun nanofibers of p-type NiO/n-type ZnO heterojunctions with enhanced photocatalytic activity, ACS Appl. Mater. Interfaces 2 (2010).

[46] J. Jiang, X. Zhang, P. Sun, L. Zhang, ZnO/BiOI heterostructures: photoinduced charge-transfer property and enhanced visible-light photocatalytic activity, J. Phys. Chem. C 115 (2011).

[47] D. Li, X. Jiang, Y. Zhang, B. Zhang, C. Pan, A novel route to ZnO/TiO2 heterojunction composite fibers, J. Mater. Res. 28 (2013).

[48] A. Das, P.M. Kumar, M. Bhagavathiachari, R.G. Nair, Hierarchical ZnO-TiO2 nanoheterojunction: a strategy driven approach to boost the photocatalytic performance through the synergy of improved surface area and interfacial charge transport, Appl. Surf. Sci. 534 (2020).

[49] H.M. Mousa, J.F. Alenezi, I.M.A. Mohamed, A.S. Yasin, A.F.M. Hashem, A. Abdal-hay, Synthesis of TiO2@ZnO heterojunction for dye photodegradation and wastewater treatment, J. Alloys Compd. 886 (2021).

[50] H. Ling, L.P. Yeo, Z. Wang, X. Li, D. Mandler, S. Magdassi, et al., TiO2-WO3 core-shell inverse opal structure with enhanced electrochromic performance in NIR region, J Mater Chem C Mater 6 (2018).

[51] Y. Xie, R. Xing, Q. Li, L. Xu, H. Song, Three-dimensional ordered ZnO-CuO inverse opals toward low concentration acetone detection for exhaled breath sensing, Sensor. Actuator. B Chem. 211 (2015).

[52] Y. Chen, H. Yan, B. Yang, Y. Lv, M. Wen, J. Xu, et al., Fabrication and optical properties of Cu2O-ZnO composite opal, Appl. Phys. Mater. Sci. Process 98 (2010).

[53] Q. Li, C. Yang, Facile fabrication of Ag3PO4 supported on ZnO inverse opals for enhancement of solar-driven photocatalysis, Mater. Lett. 199 (2017).

[54] Q. Liu, R. Mo, X. Li, S. Yang, J. Zhong, H. Li, Cobalt phosphate modified 3D TiO 2/BiVO 4 composite inverse opals photoanode for enhanced photoelectrochemical water splitting, Appl. Surf. Sci. 464 (2019).

[55] Q. Zhou, P. Dong, B. Cheng, Fabrication of SiO2/TiO2 and SiO2/Al2O3 composite inverse opals, J. Cryst. Growth 292 (2006).

[56] H. Zhang, C. Cheng, Three-Dimensional FTO/TiO2/BiVO4 composite inverse opals photoanode with excellent photoelectrochemical performance, ACS Energy Lett. 2 (2017).

[57] Z. Wang, X. Li, H. Ling, C.K. Tan, L.P. Yeo, A.C. Grimsdale, et al., 3D FTO/FTO-Nanocrystal/TiO2 composite inverse opal photoanode for efficient photoelectrochemical water splitting, Small 14 (2018).

[58] H.N. Kim, J.H. Moon, ZnO-treated TiO2 inverse opal electrodes for dye-sensitized solar cells, Curr. Appl. Phys. 13 (2013).

[59] J. Liu, C. Sun, M. Fu, J. Long, D. He, Y. Wang, Enhanced photochemical catalysis of TiO2 inverse opals by modification with ZnO or Fe2O3 using ALD and the hydrothermal method, Mater. Res. Express 5 (2018).

[60] J. Xu, B. Yang, Z. Fu, M. Wen, Y. Zhao, Synthesis and photocatalytic property of ZnO/TiO2 inverse opals films with controllable composition and topology, Chin. J. Chem. Phys. 25 (2012) 235–241.

[61] M. Pavlenko, K. Siuzdak, E. Coy, K. Załęski, M. Jancelewicz, I. Iatsunskyi, Enhanced solar-driven water splitting of 1D core-shell Si/TiO2/ZnO nanopillars, Int. J. Hydrogen Energy 45 (2020).

[62] Y. Jia, X. Li, C. Chen, W. Fang, Y. Chen, L. Wang, et al., Heterojunction engineering decorated TiO2/ZnO three-dimensional hierarchical structure with g-C3N4 for solar driving water splitting, J. Am. Ceram. Soc. 107 (2024).

[63] S.A. Mousa, H. Abdallah, S.A. Khairy, Low-cost photocatalytic membrane modified with green heterojunction TiO2/ZnO nanoparticles prepared from waste, Sci. Rep. 13 (2023).

[64] P.J. Navarro-Gazquez, M.J. Munoz-Portero, E. Blasco-Tamarit, R. Sanchez-Tovar, J. García-Anton, Synthesis and applications of TiO2/ZnO hybrid nanostructures by ZnO deposition on TiO2nanotubes using electrochemical processes, Rev. Chem. Eng. (2022).

[65] P. Akhter, S. Nawaz, I. Shafiq, A. Nazir, S. Shafique, F. Jamil, et al., Efficient visible light assisted photocatalysis using ZnO/TiO2 nanocomposites, Mol. Catal. 535 (2023).

[66] A. Mirzapoor, E. Ghashghaee, Nano engineered synthesis layer by layer and transparent synergistic antimicrobial coating based on Se/Ag/TiO2/ZnO hybrid nanostructures, Inorg. Chem. Commun. 153 (2023).

[67] J.P. Niemela, G. Marin, M. Karppinen, Titanium dioxide thin films by atomic layer deposition: a review, Semicond. Sci. Technol. (2017).

[68] J. Zhang, P. Zhou, J. Liu, J. Yu, New understanding of the difference of photocatalytic activity among anatase, rutile and brookite TiO2, Phys. Chem. Chem. Phys. 16 (2014) 20382–20386.

[69] M. Heikkila, F. Puukilainen, M. Ritala, M. Leskela, Effect of thickness of ALD grown TiO2 films on photoelectrocatalysis, J. Photochem. Photobiol. Chem. 204 (2009).

[70] J. Malm, E. Sahramo, J. Perala, T. Sajavaara, M. Karppinen, Low-temperature atomic layer deposition of ZnO thin films: control of crystallinity and orientation, Thin Solid Films (2011).

[71] A.A. Chaaya, R. Viter, M. Bechelany, Z. Alute, D. Erts, A. Zalesskaya, et al., Evolution of microstructure and related optical properties of ZnO grown by atomic layer deposition, Beilstein J. Nanotechnol. 4 (2013) 690–698.

[72] T.V. Lidiya, K. Rajeev Kumar, Spectroscopic analysis of ultrathin amorphous ZnO films grown by atomic layer deposition, Mater Today Proc (2021).

[73] K.H. Park, G.D. Han, B.J. Kim, E.H. Kang, J.S. Park, J.H. Shim, et al., Effects of atomic layer deposition conditions on the formation of thin ZnO films and their photocatalytic characteristics, Ceram. Int. 45 (2019) 18823–18830.

[74] K. Lee, M.D. Losego, D.H. Kim, G.N. Parsons, High performance photocatalytic metal oxide synthetic bi-component nanosheets formed by atomic layer deposition, Mater. Horiz. 1 (2014).

[75] N. Li, Y. Tian, J. Zhang, Z. Sun, J. Zhao, J. Zhang, et al., Precisely-controlled modification of PVDF membranes with 3D TiO2/ZnO nanolayer: enhanced anti-fouling performance by changing hydrophilicity and photocatalysis under visible light irradiation, J. Membr. Sci. 528 (2017).

[76] P. Kumari, N. Bahadur, X.A. Conlan, X. Zeng, L. Kong, L.A. O'Dell, et al., Stimuli-responsive heterojunctions based photo-electrocatalytic membrane reactors for reactive filtration of persistent organic pollutants, Chem. Eng. J. 452 (2023) 139374.

[77] M. Polat Gonullu, Cergel M. Soyleyici, H.I. Efkere, H. Ates, Investigations of some physical properties of ALD growth ZnO films: effect of crystal orientation on photocatalytic activity, J. Mater. Sci. Mater. Electron. 32 (2021).

[78] J. Rodríguez-López, R. Rangel, D. Berman-Mendoza, A. Ramos-Carrazco, J. J. Alvarado, Evaluating the response of nitrogen implantation in ZnO ALD thin films and their photocatalytic assessment, J. Photochem. Photobiol. Chem. 433 (2022) 114211.

[79] L. Lopez, W.A. Daoud, D. Dutta, B.C. Panther, T.W. Turney, Effect of substrate on surface morphology and photocatalysis of large-scale TiO 2 films, Appl. Surf. Sci. 265 (2013).

[80] Y. Paz, A. Heller, Photo-oxidatively self-cleaning transparent titanium dioxide films on soda lime glass: the deleterious effect of sodium contamination and its prevention, J. Mater. Res. 12 (1997).
[81] H.J. Nam, K. Itoh, M. Murabayashi, Photocatalytic activity of TiO2 thin film - effect of substrate, Electrochemistry 70 (2002).
[82] T.P. Chou, Q. Zhang, G. Cao, Effects of dye loading conditions on the energy conversion efficiency of ZnO and TiO2 dye-sensitized solar cells, J. Phys. Chem. C 111 (2007).
[83] J. Guo, S. Yuan, Y. Yu, J.R. van Ommen, H. van Bui, B. Liang, Room-temperature pulsed CVD-grown SiO2 protective layer on TiO2 particles for photocatalytic activity suppression, RSC Adv. 7 (2017).
[84] V. Roge, J. Didierjean, J. Crepelliere, D. Arl, M. Michel, I. Fechete, et al., Tuneable functionalization of glass fibre membranes with ZnO/SnO2 heterostructures for photocatalytic water treatment: effect of SnO2 coverage rate on the photocatalytic degradation of organics, Catalysts 10 (2020) 733.
[85] Z. Liwu, C. Hanyun, Z. Ruilong, Z. Yongfa, Photocorrosion suppression of ZnO nanoparticles via hybridization with graphite-like carbon and enhanced photocatalytic activity, J. Phys. Chem. C 113 (2009).
[86] K. Sridharan, E. Jang, Y.M. Park, T.J. Park, Superior photostability and photocatalytic activity of ZnO nanoparticles coated with ultrathin TiO2 layers through atomic-layer deposition, Chem. Eur J. 21 (2015).
[87] L.P. Bakos, N. Justh, S.B. da Costa Ucm da, K. Laszlo, J.L. Labár, T. Igricz, et al., Photocatalytic and gas sensitive multiwalled carbon nanotube/Tio2-Zno and Zno-Tio2 composites prepared by atomic layer deposition, Nanomaterials 10 (2020).
[88] S.I. Boyadjiev, O. Keri, P. Bardos, T. Firkala, F. Gaber, Z.K. Nagy, et al., TiO2/ZnO and ZnO/TiO2 core/shell nanofibers prepared by electrospinning and atomic layer deposition for photocatalysis and gas sensing, Appl. Surf. Sci. 424 (2017) 190–197.
[89] C. Cheng, A. Amini, C. Zhu, Z. Xu, H. Song, N. Wang, Enhanced photocatalytic performance of TiO2-ZnO hybrid nanostructures, Sci. Rep. 4 (2014).
[90] H. Xia, W. Zhang, Z. Yang, Z. Dai, Y. Yang, Spectrophotometric determination of p -nitrophenol under ENP interference, J Anal Methods Chem. 2021 (2021).
[91] V.V. Kadam, S.D. Shanmugam, J.P. Ettiyappan, R.M. Balakrishnan, Photocatalytic degradation of p-nitrophenol using biologically synthesized ZnO nanoparticles, Environ. Sci. Pollut. Control Ser. 28 (2021).
[92] B. Zhao, G. Mele, I. Pio, J. Li, L. Palmisano, G. Vasapollo, Degradation of 4-nitrophenol (4-NP) using Fe-TiO2 as a heterogeneous photo-Fenton catalyst, J. Hazard Mater. 176 (2010).
[93] O. Keri, L. Kocs, Z. Horvolgyi, Z. Baji, K. Laszlo, V. Takats, et al., Photocatalytically active amorphous and crystalline TiO2 prepared by atomic layer deposition, Periodica Polytechnica Chemical Engineering 63 (2019).
[94] P.L. Gareso, Juarlin E. Musfitasari, Optical and structural characterization of ZnO/TiO2 bilayer thin films grown by sol-gel spin coating, J Phys Conf Ser (2018).
[95] R. Abdul Rahman, M.A. Zulkefle, M. Rusop, W.F.H. Abdullah, S.H. Herman, Annealing temperature effect on the electrical characteristics and pH sensitivity of TiO2/ZnO bilayer films. 2nd International Symposium on Technology Management and Emerging Technologies, ISTMET 2015 - Proceeding, 2015.
[96] G.V. Aguilar, M.R.J. Fonseca, A.M. Ramírez, A.G.J. Gracia, Photoluminescence studies on ZnO thin films obtained by sol-gel method, Recent Applications in Sol-Gel Synthesis (2017).
[97] L. Gao, F. Netzaoui, F. Marty, M. Erfan, S. Bastide, Y. Leprince-Wang, et al., Tio2-coated zno nanowire arrays: a photocatalyst with enhanced chemical corrosion resistance, Catalysts 11 (2021).
[98] N.S. Bhaskar, A.D. Kadam, J.J. Biwal, P.M. Diwate, R.R. Dalbhanjan, D. D. Mahale, et al., Removal of Rhodamine 6G from wastewater using solar irradiations in the presence of different additives, Desalination Water Treat. 57 (2016).
[99] D. Roy, S. Neogi, S. De, Highly efficient reduction of p-Nitrophenol by sodium borohydride over binary ZIF-67/g-C3N4 heterojunction catalyst, J. Environ. Chem. Eng. 9 (2021).
[100] G.D. Lee, Y.J. Do, S.S. Park, S.S. Hong, Effect of hydrogen peroxide on the photocatalytic decomposition of 4-nitrophenol over TiO2/Cr-Ti- MCM-41 catalysts in visible light, Mater. Sci. Forum (2005).
[101] A.N.M.B. El-hoshoudy, Emulsion polymerization mechanism, Recent Research in Polymerization (2018).
[102] D.C. Blackley, Emulsion polymerization and its applications in industry, Polymer (Guildf). 24 (1983).
[103] J.L. Russell, G.H. Noel, J.M. Warren, N.L.L. Tran, T.E. Mallouk, Binary colloidal crystal films grown by vertical evaporation of silica nanoparticle suspensions, Langmuir 33 (2017) 10366–10373.
[104] H. Yang, P. Jiang, Large-scale colloidal self-assembly by doctor blade coating, Langmuir 26 (2010).
[105] W. Li, C. Zhang, D. Lan, W. Ji, Z. Zheng, Y. Wang, Imbibition-induced ultrafast assembly and printing of colloidal photonic crystals, J. Colloid Interface Sci. 624 (2022).
[106] K.S. Napolskii, N.A. Sapoletova, D.F. Gorozhankin, A.A. Eliseev, D.Y. Chernyshov, D.V. Byelov, et al., Fabrication of artificial opals by electric-field-assisted vertical deposition, Langmuir 26 (2010).
[107] Y. Wang, Y. Zhang, Y. Guan, Y. Zhang, Magnetic field-assisted fast assembly of microgel colloidal crystals, Langmuir 38 (2022).
[108] C. Zhang, W. Li, Y. Wang, Ultrafast self-assembly of colloidal photonic crystals during low-pressure-assisted evaporation of droplets, J. Phys. Chem. Lett. 13 (2022).
[109] E. Erdik, ORGANOZINC REAGENTS in ORGANIC SYNTHESIS. ORGANOZINC REAGENTS in ORGANIC SYNTHESIS, 2020.
[110] M. Ritala, J. Niinisto, Industrial applications of atomic layer deposition, ECS Trans. 25 (2019) 641–652.
[111] S. Seo, S. Jeong, H. Park, H. Shin, N.G. Park, Atomic layer deposition for efficient and stable perovskite solar cells, Chem. Commun. (2019).
[112] D.M. Fryauf, A.C. Phillips, M.J. Bolte, A. Feldman, G.S. Tompa, N.P. Kobayashi, Scaling atomic layer deposition to astronomical optic sizes: low-temperature aluminum oxide in a meter-sized chamber, ACS Appl. Mater. Interfaces 10 (2018).
[113] P. Poodt, R. Knaapen, A. Illiberi, F. Roozeboom, A. van Asten, Low temperature and roll-to-roll spatial atomic layer deposition for flexible electronics, J. Vac. Sci. Technol. A: Vacuum, Surfaces, and Films 30 (2012).
[114] C Te Hsieh, J.K. Chang, R.S. Juang, C.H. Chao, W.J. Ke, Y.F. Lin, et al., Roll-to roll atomic layer deposition of titania nanocoating on thermally stabilizing lithium nickel cobalt manganese oxide cathodes for lithium ion batteries, ACS Appl. Energy Mater. 3 (2020).
[115] K. Kik, B. Bukowska, P. Sicińska, Polystyrene nanoparticles: sources, occurrence in the environment, distribution in tissues, accumulation and toxicity to various organisms, Environmental Pollution (2020).
[116] R. Qiao, M. Mortimer, J. Richter, B. Rani-Borges, Z. Yu, M. Heinlaan, et al., Hazard of polystyrene micro and nanospheres to selected aquatic and terrestrial organisms, Sci. Total Environ. (2022).
[117] B. Liu, T. Li, W. Wang, L.M.C. Sagis, Q. Yuan, X. Lei, et al., Corncob cellulose nanosphere as an eco-friendly detergent, Nat. Sustain. 3 (2020).
[118] A.I. Osman, Y. Zhang, M. Farghali, A.K. Rashwan, A.S. Eltaweil, E.M. Abd El-Monaem, et al., Synthesis of green nanoparticles for energy, biomedical, environmental, agricultural, and food applications: a review, Environ. Chem. Lett. (2024).
[119] M. Weber, N. Boysen, O. Graniel, A. Sekkat, C. Dussarrat, P. Wiff, et al., Assessing the environmental impact of atomic layer deposition (ALD) processes and pathways to lower it, ACS Materials Au 3 (2023).
[120] R.A. Sheldon, Green solvents for sustainable organic synthesis: state of the art, Green Chem. (2005).
[121] D. Dworschak, C. Brunnhofer, M. Valtiner, Photocorrosion of ZnO single crystals during electrochemical water splitting, ACS Appl. Mater. Interfaces 12 (2020).
[122] Y. Yang, Y. Ling, G. Wang, T. Liu, F. Wang, T. Zhai, et al., Photohole induced corrosion of titanium dioxide: mechanism and solutions, Nano Lett. 15 (2015).
[123] B. Weng, M.Y. Qi, C. Han, Z.R. Tang, Y.J. Xu, Photocorrosion inhibition of semiconductor-based photocatalysts: basic principle, current development, and future perspective, ACS Catal. (2019).